

Coupling the Corrosion- and Pressure-Assisted Stress Buildup within the Zirconium in PWR Pipes

Asghar Aryanfar^{*†‡}, Abdel Rahman El Tallis[†], Jaime Marian[§]

[†] *American University of Beirut, Riad El-Solh, Lebanon 1107 2020*

[‡] *Bahçeşehir University, 4 Çırağan Cad, Beşiktaş, Istanbul, Turkey 34349*

[§] *University of California Los Angeles, 400 Westwood Plaza, Los Angeles, CA, 90095*

Accepted in **JOM**(Q_1) on August 29, 2022.)

Abstract

We develop a new real-time framework for **calculating the** simultaneous accumulation of **oxidation-induced** and the internal/external fluid stresses **during the corrosion of the zirconium metal** Zr . **In order to track such interfacial stress when the zirconium metal turns oxide**, we quantify the hypothetical real-time infiltration of the oxygen within the metal matrix in the curved boundary, leading to the augmentation in the volume and we compute stoichiometrically the resulted equivalent oxide thickness. Subsequently, we calculate the accumulated compressive stress in real-time from both irreversible (plastic) and reversible (elastic) events which could be used for anticipation of the onset of failure. The developed analytical framework could quantify the design parameters for **the** safe operation of **high-pressure** pipes in corrosive environments.

Keywords: Corrosion Stress, Elastic Stress, Curved Boundary, Inner/Outer Corrosion, Mechanical Failure.

1 Introduction

The oxidation of the **metallic pipelines** in the cooling section of the light water reactors (LWR) is a crucial factor for the safety assessment and engineering of their material, structural properties [1, 2] and operational process [3]. In particular, the zirconium Zr has a substantial potential **for utilization as a clad**, to withstand loads under highly oxidative regimes; however **the chemical and mechanical extent** that it **can resist** to the oxidation sets limitation on the reactor's fuel energy extraction rate [4, 5, 6, 7].

One of the main failure mechanisms in the light water reactor (LWRs) pipes is the stress buildup and the formation of a metal oxide layer, interfacing with the underlying metal [8]. **There are several**

^{*}Corresponding author, Email: aryanfar@caltech.edu

studies on the stress corrosion cracking [9, 10] and failure [11, 12], rate of crack growth [13], and role of grain orientation [14]. In particular, phase-field models have recently been developed for coupling the mechano-chemical effects [15] and dissolution-driven failure [16].

The corrosion event, in fact, corrosion succeeds the diffusion of oxygen solute from the water into the metal matrix [17, 18, 19], and since the two stages occur in series the one causing lower corrosion rate will be controlling. Typically the rate of the oxide growth starts the highest in the metal surface and reduces in time, as the oxide gets thicken and hinders the further diffusion of oxygen in deeper layer, which causes the oxidation interface *breathe* harder. However after certain achieved oxide thickness it partially breaks due to compressive stress and chemical degradation, leading to sudden jump in the oxidation rate, as the oxygen (i.e. water) could penetrate within the cracks in the oxidation surface. This pattern gets repeated and forms a series of oxidative reactions which induces a weakened structure of the overall pipe surface, leading to the susceptibility to total fracture [20, 21, 22]. The kinetics of such reactions have already been explored previously, with the focus on material composition and chemistry [23, 24, 25, 26]. The typical increase in the structure's volume is mainly attributed to the Pillar-Bedworth ratio, which translates into the added compressive stresses [27, 28, 29].

Several factors may complicate the corrosion, such as irradiation [30], pressure, temperature [31] and chemical kinetics from the side reactions [32, 23] as well as (sub)-stoichiometric (partial) oxidation [33] and hydration [34].

Experiment-wise, previous studies have explored the corrosion mechanism [35], have used microscopy (optical, SEM, Raman) [36, 37] and visual inspection [38], set up a new device [39], explored the role of environmental sulfide [40] and other additives such as fluorine [41], iodine [42], synthesized composites [43, 44], used graphene coating to enhance thermal stability [45], investigated chemical degradation in plastics [46] as well as cyclic cooling [47].

Pressure, among others, is a driving force for the diffusion of oxygen into the metal, which results in the additional stress build up [27, 48, 49]. It has previously been investigated in both atomic [50] and continuum [51] scales, where the generated compressive stress weakens the enveloping metal material and expedites the failure [52]. Having such importance, the pressure-dependent research on corrosion lacks sufficiency, particularly in terms of coupling with the corrosion-induced internal stresses.

In this paper, a one dimensional pressure-induced corrosion kinetics model has been developed in the cylindrical pipelines [53, 54, 55, 56]. The diffusion of oxygen from both concentration gradient [57] and the external mechanical pressure [58, 59] is quantified and the equivalent oxide thickness is anticipated. Subsequently, we have developed a framework to compute the resulted effective mechanical compressive stress within the oxidized medium. The developed methodology is useful for designing the range of the parameters for avoiding the failure of the PWR cooling pipelines.

Table 1: Model Parameters.

| Variables | | | | Constants | | | |
|---------------|-------------------------|-----------------|----------------------|-----------|------------------------|---------------------|------------|
| Par. | Values | Unit | Ref. | Par. | Value | Unit | Ref. |
| D | 1.4×10^{-20} , | $m^2.s^{-1}$ | [60] | k_B | 1.38×10^{-23} | $J.K^{-1}$ | [61] |
| M | 123 | $g.mol^{-1}$ | [62] | N_A | 6.02×10^{23} | $atom.mol^{-1}$ | [63] |
| R_{PB} | 1.56 | [] | [64, 28] | R_u | 8.314 | $J.mol^{-1}.K^{-1}$ | [63] |
| K | 142 | GPa | Azom ¹ | P_O | 15 | MPa | [65] |
| k | 7.1×10^{-6} | s^{-1} | [66] | P_I | 110 | MPa | [67] |
| f | 0.3 | [] | [68, 51] | R_O | 2.5 | mm | [69] |
| ν | 0.34 | [] | [70] | R_I | 1.5 | mm | [69] |
| T | 630 (357) | $K (^{\circ}C)$ | [33] | C_0 | 55×10^3 | $mol.m^{-3}$ | Equation 2 |
| σ_{uc} | 1200 | MPa | Azom ^{1, 2} | dr | 4×10^{-4} | m | Assumed |
| Ω | 2.2×10^{-5} | $m^3.mol^{-1}$ | Equation 1 | dt | 1.7×10^{12} | s | Calculated |

2 Methodology

2.1 Material Properties

The material properties for the framework are expressed in the Table 1, which are mainly extracted for the zirconium Zr with the pressurized water. While most of the variables/constants are the typical values from the references, the rest are calculated. For instance, the molar volume Ω is calculated via molar mass M and the mass density ρ as:

$$\Omega = \frac{M}{\rho} = \frac{123g.mol^{-1}}{5.68g.cm^{-3}} \approx 22 \times 10^{-6}m^3.mol^{-1} \quad (1)$$

As well the oxygen concentration in the water C_0 is simply obtained as:

$$C_0 = \frac{\rho}{M} = \frac{1000gr.L^{-1}}{18gr.mol^{-1}} = 55mol.L^{-1} \quad (2)$$

2.2 Framework

During the corrosion event, the infiltration of oxygen within the metal and the subsequent reaction leads to the formation of the oxide layer on the surface of the metal. Figure 1a shows such formation in our experimental sample. In pipe geometry, this could occur either in the inner or outer boundary of the pipes as shown in the Figure 1b with the distinguishing colors.

During the growth of the thin oxide layer on top of the underneath metallic medium, while the radial boundaries (R_I , R_O) remain free to move, the lateral (i.e. hoop) boundaries, remain constrained, the misfit stress σ_{EL} builds on due to volumetric difference between the oxide and metal.

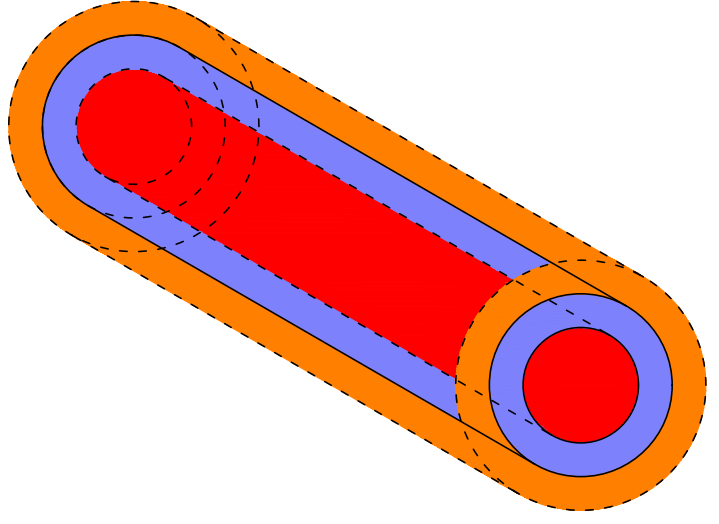
Additionally, in the same direction, the hoop component of the pressure-induced stress σ_{θ} from the

¹<https://www.azom.com/properties.aspx?ArticleID=133>

²For conservative purpose, the minimum value is considered.



(a) Sample of lab-scale formation of corrosion layers on both internal and external surfaces.



(b) The pipe (blue) with the imposed inner (orange) and outer (red) pressure flows.

Figure 1: The experimental sample of the corroded pipe (left) and the schematics of the internal/external flows (right).

internal/external fluid will be a contributing factor in the same direction. Therefore, the total stress σ_{Tot} would be their sum as shown in the Equation 3:

$$\sigma_{Tot} = \sigma_{EL} + \sigma_{\theta} \quad (3)$$

and we explain each stress term separately as below:

2.2.1 Elastic Stress σ_{EL}

Imposing the internal and external pressures P_I and P_O , the radial σ_r and hoop σ_{θ} elastic stresses develop, as shown in the Figure 2a which are only function of radius r due to polar symmetry. Cutting-out the infinitesimal element shown in the Figure 2b the balance relationships in horizontal direction is obtained in the Equation 4 as [71]:

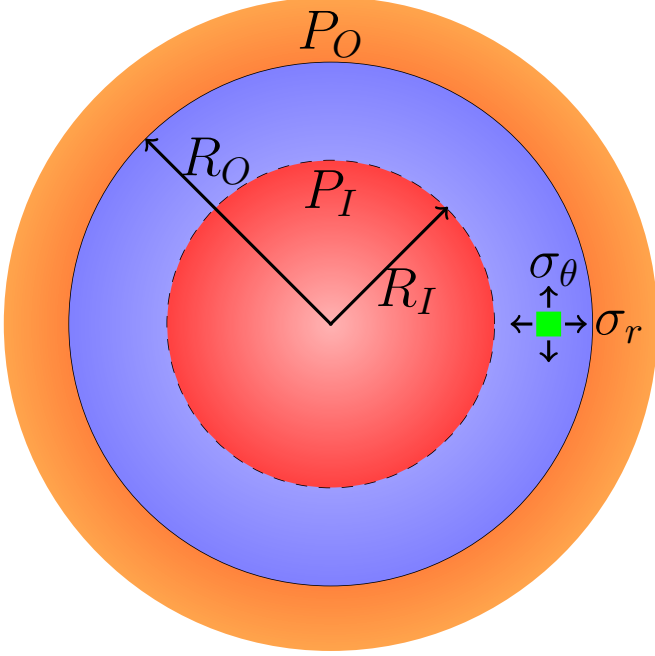
$$\left(\sigma_r + \frac{\partial \sigma_r}{\partial r} dr \right) \cdot (r + dr) d\theta - \sigma_r \cdot r d\theta - 2\sigma_{\theta} \cdot dr \cdot \frac{d\theta}{2} = 0 \quad (4)$$

where by simplification and ignoring the higher orders terms, we arrive at Lamé's relationship as [72]:

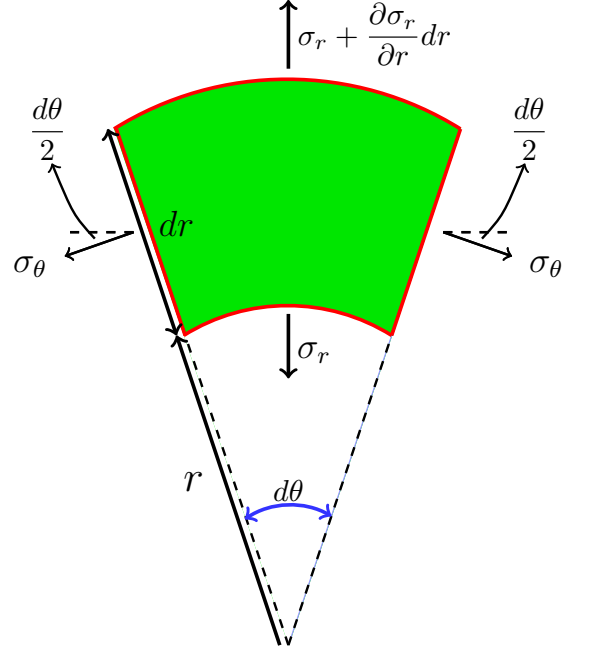
$$\frac{\partial \sigma_r}{\partial r} + \frac{\sigma_r - \sigma_{\theta}}{r} = 0 \quad (5)$$

Considering u as the infinitesimal displacement in the radial direction, solving for the radial σ_r and hoop σ_{θ} stresses, one gets ([71], App. 1):

$$\begin{cases} \sigma_r = \frac{E}{1 - \nu^2} \left(\frac{du}{dr} + \nu \frac{u}{r} \right) \\ \sigma_{\theta} = \frac{E}{1 - \nu^2} \left(\frac{u}{r} + \nu \frac{du}{dr} \right) \end{cases} \quad (6)$$



(a) Cross-sectional schematic of the medium with the resulted hoop (σ_θ) and radial (σ_r) stresses



(b) The infinitesimal element analyzed for stress equilibrium.

Figure 2: Characterization of the stresses and equilibrium forces.

From the Figure 2a, assuming the $\{R_I, R_O\}$ are inner and outer radii the pipe respectively and assigning the boundary conditions for the compressive stresses as $\sigma_r(R_I) = -P_I$ and $\sigma_r(R_O) = -P_O$, the hoop stress σ_θ is finally obtained in Equation 7 as (App. 1):

$$\sigma_\theta = \frac{P_I R_I^2 - P_O R_O^2}{R_O^2 - R_I^2} + \left(\frac{R_I^2 R_O^2 (P_O - P_I)}{R_O^2 - R_I^2} \right) \frac{1}{r^2} \quad (7)$$

which is the compressive stress generated by the bounded-ness in the azimuthal (i.e hoop) direction.

2.2.2 Corrosion Stress σ_{PL}

Figure 3 illustrates the infinitesimal variation in the volumes by means of the superposition. In the absence of the underneath metallic medium the oxidation would lead to the free expansion (shown in Green). However, due to boundedness from the azimuthal (hoop) direction, the horizontal expansion would translate into additional radial expansion via Poisson's effect (shown in Red). As given in the Equation 8 any swelling in the surface δr , is partially the result of the natural oxidation with plastic irreversible deformation δr_{PL} as well as the straining due to elastic lateral compressive stress (Poisson effect) δr_{EL} , as:

$$\delta r = \delta r_{PL} + \delta r_{EL} \quad (8)$$

The isotropic plastic straining can be explained in the Equation 9 as:

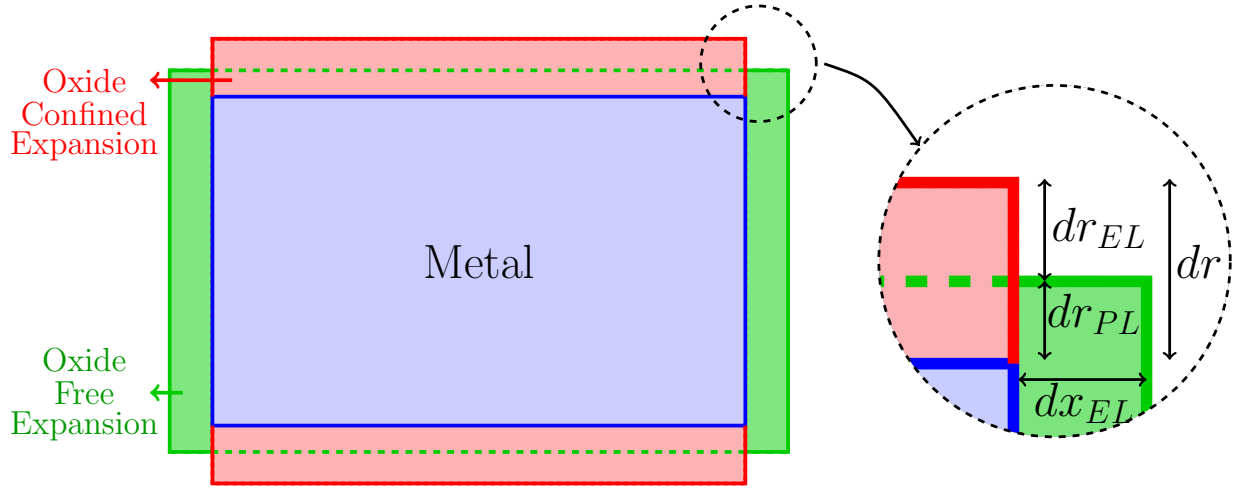


Figure 3: Swelling due to both oxidation and the lateral compressive stress. (Blue: original metal, Green: Free oxide expansion, Red: Confined oxide expansion.)

$$\frac{\delta r_{PL}}{r} = \frac{\delta x_{PL}}{x} \quad (9)$$

where x here is the hoop direction. As well, the Poisson's effect is characterized by the Equation 10 as:

$$\frac{\delta r_{EL}}{r} = \nu \frac{\delta x_{PL}}{x} \quad (10)$$

Combining Equations 8, 9 and 10 we get the elastic versus the total displacement ratio in the Equation 11 as:

$$\frac{\delta r_{EL}}{r} = \frac{\nu}{1 + \nu} \frac{\delta r}{r} \quad (11)$$

On the other hand, considering 2D augmentation (i.e. $\frac{\delta V}{V} \approx \frac{\delta A}{A} \approx \frac{\delta r}{r}$), the infinitesimal growth of the elastic compressive stress $\delta \sigma_{EL}$ would be given in the Equation 12 as:

$$\delta \sigma_{EL} \approx K \frac{\nu}{1 + \nu} \frac{dA}{A} \quad (12)$$

where the fraction $\frac{\nu}{1 + \nu}$ is the partial effect of compressive stress on the swelling. The rest of expansion is due to sole oxidation, which doesn't generate compressive stress. Therefore, the elastic compressive stress from the corrosion $\delta \sigma_{EL}$ is caused by the portion of the swelling responsible for Poisson's effect.

During the oxidation, as the oxygen diffuses into the metal matrix, an infinitesimal metallic volume δV_M is removed and gets replaced plastically by the respective oxide of higher volume δV_{PL} such that $\delta V_{PL} = R_{PB} \delta V_M$, and R_{PB} ³ is the Pilling-Bedworth ratio [74], representing the oxide-to-metal volumetric ratio. Hence, the total augmentation in the surface δr turns into their difference obtained in the Equation

³For Zirconium $R_{PB} = 1.56$ [73].

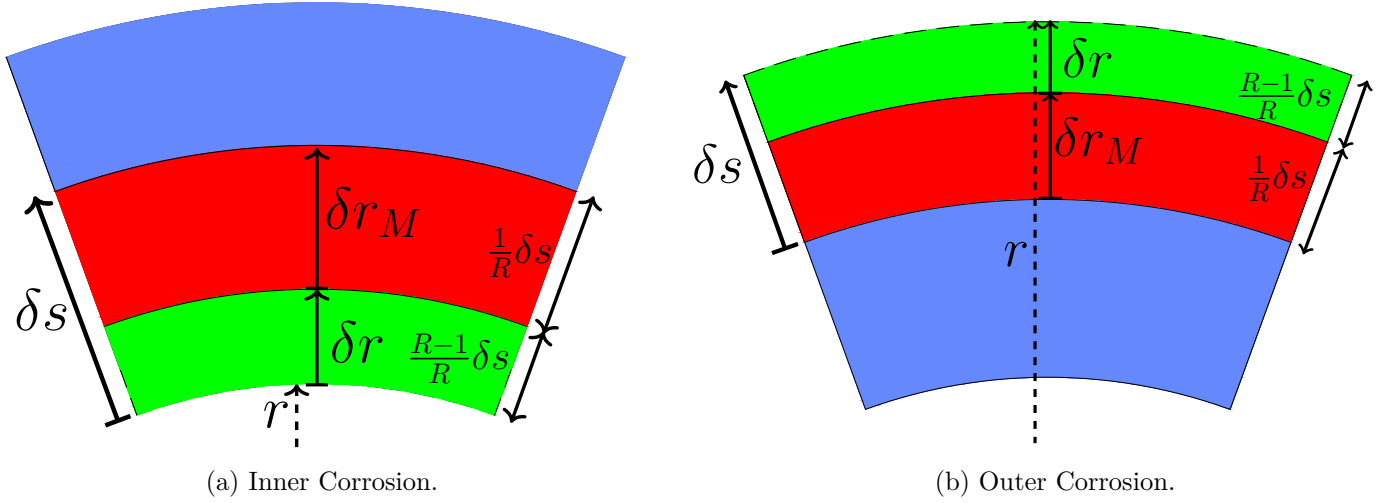


Figure 4: Schematics of the inner (a) and outer (b) corrosion: **Blue**: Metal layer, **Red**: Oxide layer, **Green**: Augmented volume due to oxidation.

13 as:

$$\begin{aligned}\delta r &= \delta s - \delta r_M \\ &= \frac{R_{PB} - 1}{R_{PB}} \delta s\end{aligned}\tag{13}$$

where the fraction $\frac{R_{PB} - 1}{R_{PB}}$ (< 1) shows the partial effect of swelling from the replacement of the metal δV_M with the larger oxide volume δV_{PL} .

Inner Corrosion

The parametrization of the inner corrosion is shown in the Figure 4a. The infinitesimal variations in the radial direction δr and the oxide thickness δs are correlated as: $\delta r = -\frac{R_{PB} - 1}{R_{PB}} \delta s$ where the negative sign represents their opposite growth pattern, hence integrating from the initial value of $r_0 = R_I$ and $s_0 = 0$ yields the Equation 14 as:

$$r = R_I - \frac{R_{PB} - 1}{R_{PB}} s\tag{14}$$

additionally, the infinitesimal oxide area change dA in the radius r is given in the Equation 15 as:

$$dA = 2\pi \left(R_I - \frac{R_{PB} - 1}{R_{PB}} s \right) \frac{R_{PB} - 1}{R_{PB}} ds\tag{15}$$

Additionally, the total oxidized area A is given in the Equation 16:

$$A = \pi \left(R_O^2 - \left(R_I - \frac{R_{PB} - 1}{R_{PB}} s \right)^2 \right) \quad (16)$$

Hence combining the Equations 12, 13, 15 and 16 we achieve the elastic stress σ_{EL} given in the equation 17 as (App. 2):

$$\sigma_{EL} = K \frac{\nu}{1 + \nu} \ln \left(1 + \frac{R_{PB} - 1}{R_{PB}} \left(\frac{2R_I}{R_O^2 - R_I^2} \right) s + \left(\frac{R_{PB} - 1}{R_{PB}} \right)^2 \frac{s^2}{R_O^2 - R_I^2} \right) \quad (17)$$

Outer Corrosion

During the outer corrosion, which is parametrized in the Figure 4b, the correlation would bet $\delta r = \frac{R_{PB} - 1}{R_{PB}} \delta s$, and δs and δr are in the same direction. Integrating from the initial values of $r_0 = R_O$ and $s_0 = 0$ we get the Equation 18:

$$r = R_O + \frac{R_{PB} - 1}{R_{PB}} s \quad (18)$$

Respectively, the infinitesimal oxide area change dA is attained in the Equation 19 as:

$$dA = 2\pi \left(R_O + \frac{R - 1}{R} s \right) \frac{R_{PB} - 1}{R_{PB}} ds \quad (19)$$

and the total oxidized area is given in the Equation 20 as:

$$A = \pi \left(\left(R_O + \frac{R_{PB} - 1}{R_{PB}} s \right)^2 - R_I^2 \right) \quad (20)$$

Therefore, combining the Equations 12, 13, 19 and 20 we get the elastic stress σ_{EL} obtained in the Equation 21 as (App. 3) :

$$\sigma_{EL} = K \frac{\nu}{1 + \nu} \ln \left(1 + \frac{R_{PB} - 1}{R_{PB}} \left(\frac{2R_O}{R_O^2 - R_I^2} \right) s + \left(\frac{R_{PB} - 1}{R_{PB}} \right)^2 \frac{s^2}{R_O^2 - R_I^2} \right) \quad (21)$$

2.2.3 Corrosion Kinetics

The corrosion consists of the two simultaneous events of *diffusion* and *reaction* which establishes a mass-balance relationship. While the diffusion event carries the oxygen atoms inside the metal, the reaction term consumes them to turn metal to the oxide. For simplicity, herein we perform superposition for the diffusion-reaction event and explore either of them individually as below:

I. Oxygen Infiltration (Diffusion)

Regarding the change in the concentration due to sole diffusion $\left(\frac{dC}{dt} \right)_{\text{Diff}}$, the rate of influx is controlled by the gradient of the oxygen concentration C and stress σ as [57, 51]:

Table 2: The boundary conditions for either inner or outer corrosion.

| Inner Corrosion (P_I) | Outer Corrosion (P_O) |
|--|--|
| $\begin{cases} C(R_I, t) = C_0 \\ \frac{\partial C(R_O, t)}{\partial r} = 0 \end{cases}$ | $\begin{cases} \frac{\partial C(R_I, t)}{\partial r} = 0 \\ C(R_O, t) = C_0 \end{cases}$ |

$$\left(\frac{dC}{dt} \right)_{\text{Diff}} = -D \nabla \cdot \left(\nabla C + \frac{f\Omega}{R_u T} C \nabla \sigma \right) \quad (22)$$

where D is the diffusion coefficient, f is the dimension-less contraction factor [68] ($0 < f < 1$), Ω is the molar volume, R_u is the universal gas constant and T is the temperature. Such relationship in the radial distance for the concentration $C(r, t)$ can be expressed as (App. 4):

$$\left(\frac{dC}{dt} \right)_{\text{Diff}} = D \frac{\partial^2 C}{\partial r^2} + \alpha(r) \frac{\partial C}{\partial r} + \beta(r) C \quad (23)$$

where $R_I < r < R_O$ and the range of time is considered as $0 < t < \sim \frac{R_O^2}{D}$. The coefficients of $\alpha(r)$ and $\beta(r)$ are obtained as (App. 4):

$$\begin{cases} \alpha(r) = -\frac{2Df\Omega B}{R_u T r^3} \\ \beta(r) = 6 \frac{f\Omega B}{R_u T r^4} \end{cases} \quad (24)$$

and the derivation is provided in the Appendix. The corresponding initial condition would be the intact metal (i.e. no oxygen) as:

$$C(r, 0) = 0 \quad (25)$$

The respective boundary conditions for either inner or outer corrosion are shown in the Table 2, where the constant boundary condition in the Table 2 shows the contact with the ambient oxygen supply whereas the zero derivative condition represents the no-escape of the oxygen from the respective interface.

Numerical Solution

The non-linear equation 23 could get numerically solved by segmenting the time and space intervals, δt and δr respectively. If C_i^j represents the time t^j and the radial distance r_i respectively, we utilize the forward move in the and space (FTFS) and re-write the Equation 23 as:

$$\frac{C_i^{j+1} - C_i^j}{\delta t} = D \frac{C_{i+1}^j + C_{i-1}^j - 2C_i^j}{\delta r^2} + \alpha(r) \frac{C_{i+1}^j - C_i^j}{\delta r} + \beta(r) C_i^j \quad (26)$$

re-arranging for the concentration values in the time gives the neighbor-dependent concentration relationship in the Equation 27 as:

Table 3: The boundary conditions for the numerical solution.

| Inner Corrosion (P_I) | Outer Corrosion (P_O) |
|--|--|
| $\begin{cases} C_1^j = C_0 \\ C_{end-1}^j = C_{end}^j \end{cases}$ | $\begin{cases} C_1^j = C_2^j \\ C_{end}^j = C_0 \end{cases}$ |

$$C_i^{j+1} = Q_1 C_i^j + Q_2 C_{i+1}^j + Q_3 C_{i-1}^j \quad (27)$$

and the Q_i s are the quotients extracted as below in the Equation 28:

$$\begin{cases} Q_1 = 1 - \frac{2D\delta t}{\delta r^2} + \frac{\alpha(r)\delta t}{\delta r} + \beta(r)\delta t \\ Q_2 = \frac{\alpha(r)\delta t}{D\delta t} \\ Q_3 = \frac{D\delta t}{\delta r^2} \end{cases} \quad (28)$$

As well, the boundary conditions in the Table 2 are translated into the Table 3.

Hence, the resolution criterion is obtained conservatively as (App. 5):

$$\delta t < \left(\frac{2D}{\delta r^2} + \frac{2fD\Omega B}{R_u T r^3 \delta r} - \frac{6fD\Omega B}{R_u T r^4} \right)^{-1} \quad (29)$$

In order enlarge the application to the broader ranges of scales, the dimensionless parameters are defined below by normalizing as:

$$\hat{r} = \frac{r - R_I}{R_O - R_I}, \hat{C} = \frac{C}{C_0}, \hat{t} = \frac{D}{R_O^2} t, \hat{s} = \frac{s}{R_O - R_I} \quad (30)$$

since $R_I \leq r \leq R_O$ and $C \leq C_0$ hence $0 \leq \hat{C}, \hat{r}, \hat{s} \leq 1$. The evolution of the concentration profile based on the parameters given in the Table 1 for either inner or outer corrosion is shown in the Figures 5a and 5b respectively.

II. Oxygen Consumption

The infiltrated oxygen gets simultaneously consumed via corrosion reaction with the rate of $\left(\frac{dC}{dt} \right)_{\text{Rxn}}$, which is obtained from [73]:

$$\left(\frac{dC}{dt} \right)_{\text{Rxn}} = -kC \quad (31)$$

where k is the reaction constant for the oxidation. Comparing the rates of the diffusion $\left(\frac{dC}{dt} \right)_{\text{Diff}}$ and

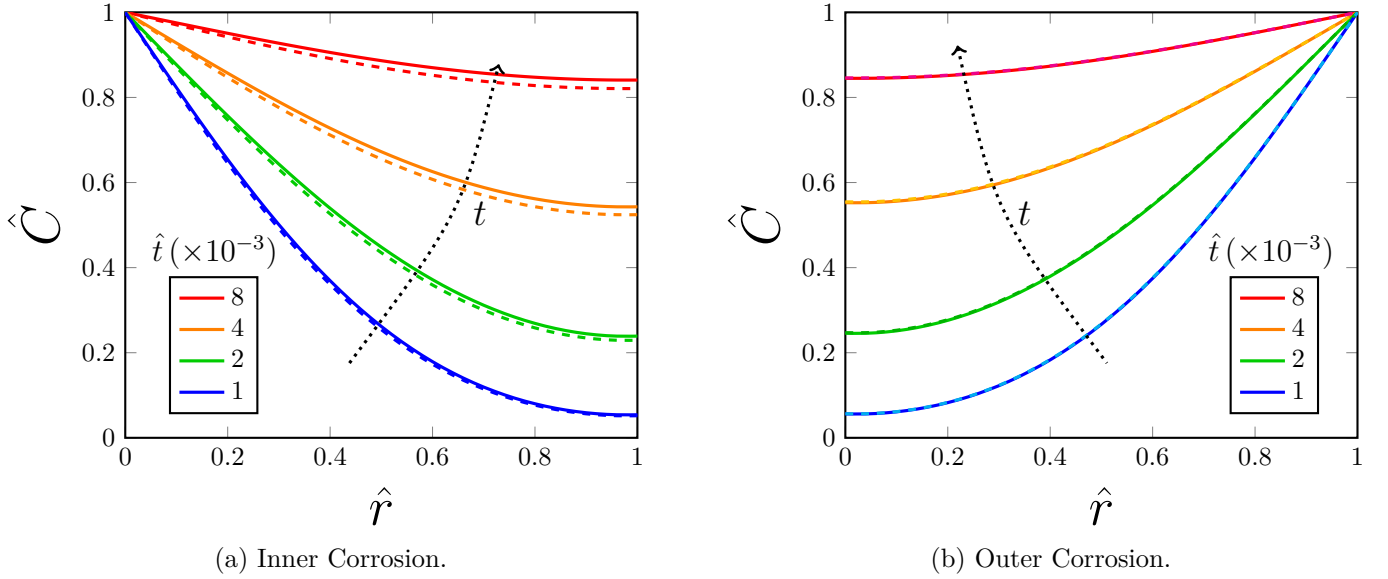


Figure 5: The evolution of *hypothetical* oxygen concentration during the inner (left) and outer (right) corrosion. The dashed lines represent the no-pressure case scenario.

reaction $\left(\frac{dC}{dt}\right)_{\text{Rxn}}$ from the realistic values given in the Table 1 we get:

$$\begin{cases} \left(\frac{dC}{dt}\right)_{\text{Diff}} \sim D \frac{C_0}{R_O} \sim 10^{-15} \text{mol.s}^{-1} \\ \left(\frac{dC}{dt}\right)_{\text{Rxn}} \sim kC_0 \sim 10^{-1} \text{mol.s}^{-1} \end{cases} \quad (32)$$

which means that, the rate of consumption is far larger than the diffusion [33], **albeit the events are simultaneous**. Therefore upon reaching the reaction sites, **the earliest event to occur is reaction** and the entire oxygen **gets** consumed to the stoichiometric **saturation**. In fact, the hypothetical concentration profiles shown in the Figures 5a and 5b **never get** stablised physically in the presence of **exceptionally large reaction rates** and the thickness of the oxide scale s **would be their reaction-equivalent case scenario**. Hence for a corrosion in the vicinity of the radial distance r , we get the equation 33 by means of mass balance:

$$s = \frac{\Omega}{2\pi r} \int_{R_I}^{R_O} C dA \quad (33)$$

where Ω is the molar volume of the oxygen, $2\pi r$ is the peripheral area of the oxidation interface in the **radial** distance r , C is the hypothetically established concentration throughout the radial range $R_I < r < R_O$ and dA is the respective infinitesimal area. Figure 6 illustrates the evolution of the oxide **thickness \hat{s} versus time \hat{t}** in dimension-less form for either inner or outer corrosion, **where the role of the location on the rate of corrosion has been emphasized**.

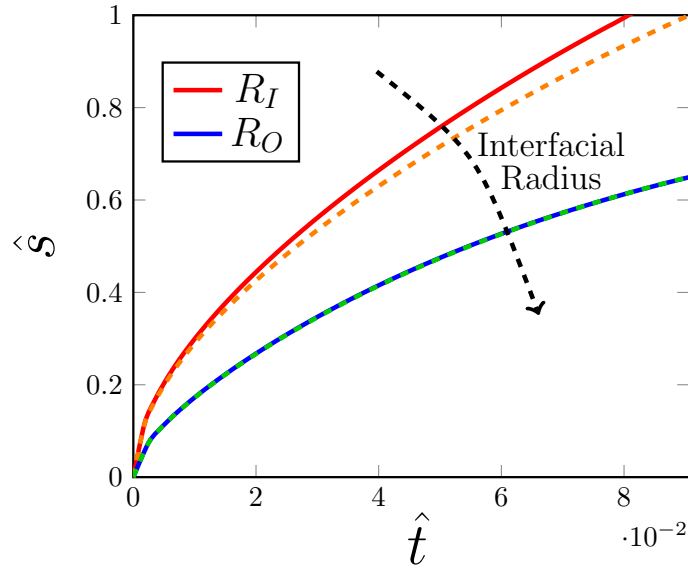


Figure 6: Evolution of the oxide thickness \hat{s} in the locations of the inner R_I and outer R_O radii (solid: with pressure, dashed: no pressure).

3 Results & Discussion

From the Figure 5 it is observed that the filling of the oxygen concentration within the medium has higher rate for the pressurized case. The underlying reason is the radial stress σ_r which directly enforces higher flux of the oxygen, than typical diffusion.

The accumulated stresses in the inner and outer corrosion based on 17 and 21 are presented within the Figure 7, and have been compared with the experimental data, which are in larger-part in close proximity of each other. The relative earlier failure of the prior could be attributed to the difference in their experimental setup and process [75, 76]. For instance, Garzarolli et. al. [77] has performed prior irradiation to the samples as well as using BWR⁴ condition, which makes a deeper (i.e. weaker) nodular oxide (vs the uniform oxidation in PWR⁵) and could fail earlier. As well Stehle et. al. [78] have considered the hydride role and orientation, which additionally contributes the failure. However the results of Hillner et. al. [69], which refer the PWR conditions, are in closer agreement with our results.

The linear appearance in these graphs shows that the fracture of the material occurs upon the formation of a thin layer where $s \ll R_O - R_I$. In fact, one can approximate the corrosion stress σ_{EL} via the Taylor expansion and ignoring the higher order terms⁶. Therefore, linearization of the Equations 17 and 21 yields the accumulated elastic stress at the given interfacial radius r as:

$$\sigma_{EL} \approx K \frac{\nu}{1 + \nu} \frac{R_{PB} - 1}{R_{PB}} \frac{2rs}{R_O^2 - R_I^2} \quad (34)$$

⁴Boiling Water Reactor (low pressure).

⁵Pressurized water reactor (high pressure).

⁶ $\ln(1 + x) \approx x - \overset{0}{O(x^2)}$ when x is small.

which means that the amount of the accumulated stress σ_{EL} is proportional to the radius of the corrosion r . Looking closer to the non-linear form of the stress in the Equations 17 and 21 it is initially obvious that $\frac{\partial \sigma_{EL}}{\partial s} > 0$. Additionally, we realize that:

$$\frac{d^2 \sigma_{EL}}{ds^2} \approx - \left(\frac{R_{PB} - 1}{R_{PB}} \right)^2 \left(\frac{2R_I}{R_O^2 - R_I^2} \right)^2 < 0 \quad (35)$$

therefore the form of the stress accumulation versus oxide thickness is concave, which becomes more apparent during extended corrosion scale. As well for the corrosion in the vicinity of a given radial distance r , the critical thickness s_c where the medium fails due to compressive stress is obtained from setting $\sigma_{EL} = \sigma_{u,c}$ in the Equation 34 as:

$$s_c = \frac{\sigma_{u,c}}{K} \frac{1 + \nu}{\nu} \frac{R_{PB}}{R_{PB} - 1} \frac{R_O^2 - R_I^2}{2r} \quad (36)$$

where $\sigma_{u,c}$ is the compressive strength of material. Furthermore, the interpretation from the Equation 36 yields:

$$r \uparrow \Rightarrow s_c \downarrow \quad (37)$$

which implies that the inner corrosion has faster rate of growth since less material is needed to generate similar oxide thickness s , as shown in the Figure 6 (i.e. since $R_O > R_I$ therefore $s_{c,O} < s_{c,I}$). Thus, having similar oxide thickness s , the amount of the accumulated stress for the outer corrosion is larger than the inner corrosion, which is reasonable since the outer boundary possess higher amount of the material leading to the compressive stress, than the inner. The main reason for the decrease in the rate of the oxide growth has been attributed to the lower accessibility of the inner regions of the corrosion to the supply of oxygen in the boundary [73], where the larger depth of oxide, the harder the corrosion interface can *breathe*.

Regarding, the variation of the critical thickness s_c versus the Poisson ratio, from Equation 36 we get:

$$\frac{\partial s_c}{\partial \nu} \sim - \frac{1}{\nu^2} < 0 \quad (38)$$

which means their inverse correlation. In fact, it is obvious that the more lateral effect imposed by the Poisson ratio, the earlier the medium breaks.

Finally, regarding the resolution criterion provided in the Equation 29, the extra terms shows the need for a finer segmentation in time δt versus the radial segmentation δr in the polar-to-planar diffusion where solely $\delta t \leq \frac{\delta r^2}{2D}$ [79]. This could be attributed to the extra term in the gradient in the polar coordinates relative to the planar coordinate, which requires more strict criterion for time versus space discretization.

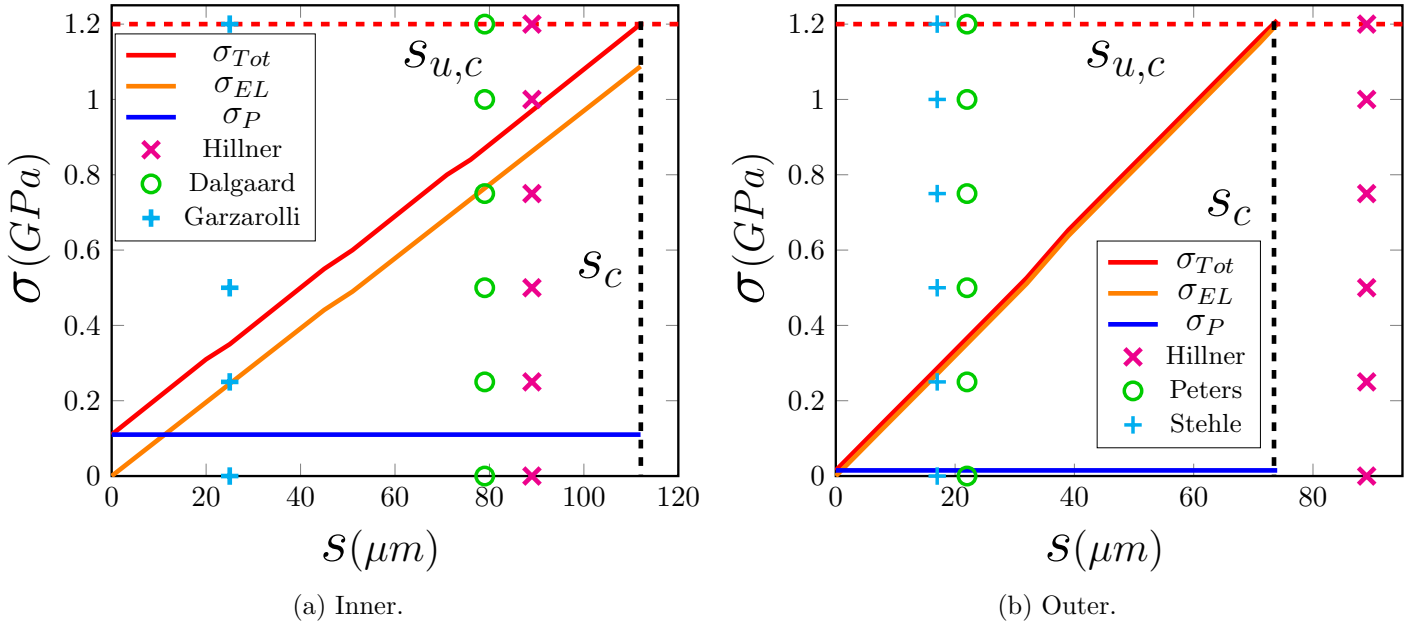


Figure 7: The stress build-up versus the thickness, illustrating the total accumulated stress at the verge of failure. The range of previous experimental findings is illustrated via the blue region.

4 Conclusion

In this paper, we have developed a time-and-thickness dependent framework for the build-up of the compressive stresses within the oxide medium via considering the fractional role of the swelling on generating the stress. As well we have coupled the resulted stress with the pressure-induced fluid pressure for either the inner or outer corrosion. Performing the superposition for the accumulation and consumption of the oxygen, we compute the diffused oxygen into the metal, we obtain the resulted equivalent oxide thickness stoichiometrically, which represents the fractional swelling of the surface via metal-removal and oxide-adding. Adding the elastic stress due to pressure as well as the corrosion effect, we use it as a measure for anticipating the onset of mechanical failure. Our formulation, which is based on the physical parameters involved, could be useful for the design and maintenance process of high-pressure pipes in aqueous environments.

Acknowledgment

The authors would like to thank the support from Masri Institute at American University of Beirut, Grant Award No. 103919 for the student Abdel Rahman El Tallis.

Data Availability

The row data for producing the results in this manuscript are freely available upon request from the corresponding author at aryanfar@caltech.edu.

Nomenclature

| | |
|---|---|
| D : Diffusion Coefficient ($m^2.s^{-1}$) | $\delta r_{PL}, \delta V_{PL}$: vertical (radial) swelling and volume change due to oxidation (m, m^3) |
| f : Dimensionless stress Factor ([]) | δr_{EL} : vertical (radial) swelling due to Poisson's effect (m) |
| Ω : Molar volume ($m^3.mol^{-1}$) | δr : total infinitesimal swelling (m) |
| T : Temperature (K) | δx_{PL} : Horizontal swelling due to oxidation (m) |
| R_u : Gas constant ($8.3J.mol^{-1}.K^{-1}$) | K : Bulk modulus (Pa) |
| R_I : Inner radius (m) | $(dt), t$: (incremental) time (s) |
| R_O : Outer radius (m) | C : Concentration of oxygen ($mol.m^{-3}$) |
| σ_{EL} : Elastic stress (Pa) | C_0 : concentratio of oxygen in water ($mol.m^{-3}$) |
| σ_{PL} : Plastic stress (Pa) | a : areal coefficient (m^2) |
| σ_r : Radial stress (Pa) | k : reaction (corrosion) constant (s^{-1}) |
| σ_θ : Hoop stress (Pa) | N_O : Moles of filled oxygen ([]) |
| σ_{Tot} : Total stress (Pa) | s : Thickness of oxide scale (m) |
| P_I : Internal Pressure (Pa) | s_c : Critical thickness of oxide scale for failure (m) |
| P_O : External Pressure (Pa) | A_{OX} : Area of oxide (m^2) |
| r : radial variable (m) | M : molar mass ($gr.mol^{-1}$) |
| E : Elastic modulus (Pa) | σ_{uc} : Ultimate compressive strength (Pa) |
| ν : Poisson's ratio ([]) | k_B : Boltzmann constant ($J.K^{-1}$) |
| $\delta V_M, \delta r_M$: Infinitesimal increase in metallic volume and thickness (m^3, m) | δV_{PL} : Infinitesimal oxide volume (m^3) |
| $s_{c,I}$: internal failure thickness (m) | R_{PB} : Pilling-bedworth ratio ([]) |
| $s_{c,O}$: external failure thickness (m) | dr : Infinitesimal radial variation (m) |
| u : infinitesimal radial displacement (m) | $d\theta$: Infinitesimal azimuthal variation ([]) |
| $(\delta V), V$: (incremental) volume (m^3) | |
| $(\delta A), A$: (incremental) area (m^2) | |

Conflict of Interest Statement

The authors declare that they have no competing financial interests to influence the work reported in this paper.

References

- [1] Neil A North and Ian D MacLeod. Corrosion of metals. In *Conservation of marine archaeological objects*, pages 68–98. Elsevier, 1987.
- [2] Hans-Henning Strehblow and Philippe Marcus. Fundamentals of corrosion. *Corrosion Mechanisms in Theory and Practice*, pages 1–104, 2012.
- [3] Donald R Knittel and Arturo Bronson. Pitting corrosion on zirconium:a review. *Corrosion*, 40(1):9–14, 1984.
- [4] Philippe Bossis, Dominique Pecheur, Karine Hanifi, Joël Thomazet, and Martine Blat. Comparison of the high burn-up corrosion on m5 and low tin zircaloy-4. In *Zirconium in the Nuclear Industry: 14th International Symposium, ASTM STP*, volume 1467, pages 494–524, 2006.

- [5] AS Zaimovskii. Zirconium alloys in nuclear power. *Soviet Atomic Energy*, 45(6):1165–1168, 1978.
- [6] Rion A Causey, Donald F Cowgill, and Robert H Nilson. Review of the oxidation rate of zirconium alloys. Report, Sandia National Laboratories, 2005.
- [7] Edward Hillner. Corrosion of zirconium-base. *Zirconium in the Nuclear Industry*, 633:211, 1977.
- [8] Arthur T Motta, Aylin Yilmazbayhan, Marcelo J Gomes da Silva, Robert J Comstock, Gary S Was, Jeremy T Busby, Eric Gartner, Qunjia Peng, Yong Hwan Jeong, and Jeong Yong Park. Zirconium alloys for supercritical water reactor applications: Challenges and possibilities. *J. Nucl. Mater.*, 371(1):61–75, 2007.
- [9] AA Kharkov, AA Alkhimenko, NO Shaposhnikov, and EL Alekseeva. Ssr method: Application to studying the mechanism of stress corrosion cracking in steels and alloys (overview). *Materials Physics & Mechanics*, 47(3), 2021.
- [10] A Contreras, M Salazar, A Albiter, R Galván, and O Vega. Assessment of stress corrosion cracking on pipeline steels weldments used in the petroleum industry by slow strain rate tests. *Arc Welding, IntechOpen Zagreb, Croatia*, page 144, 2011.
- [11] Atika Hossain Akhi and Ashutosh Sutra Dhar. Stress intensity factors for external corrossions and cracking of buried cast iron pipes. *Engineering Fracture Mechanics*, 250:107778, 2021.
- [12] Yanan Qin, Victor Litvinov, Walter Chassé, Jin Sun, and Yongfeng Men. Environmental stress cracking of polyethylene pipe: Changes in physical structures leading to failure. *Polymer*, 252:124938, 2022.
- [13] IV Ryakhovskikh and RI Bogdanov. Model of stress corrosion cracking and practical guidelines for pipelines operation. *Engineering Failure Analysis*, 121:105134, 2021.
- [14] Zhe Wang, Pingquan Wang, Dezhi Zeng, Taihe Shi, and Wenliang Deng. A study on the influential factors of stress corrosion cracking in c110 casing pipe. *Materials*, 15(3):801, 2022.
- [15] Chen Lin and Haihui Ruan. Phase-field modeling of mechano–chemical-coupled stress-corrosion cracking. *Electrochimica Acta*, 395:139196, 2021.
- [16] Chuanjie Cui, Rujin Ma, and Emilio Martínez-Pañeda. A phase field formulation for dissolution-driven stress corrosion cracking. *Journal of the Mechanics and Physics of Solids*, 147:104254, 2021.
- [17] B Cox. Some thoughts on the mechanisms of in-reactor corrosion of zirconium alloys. *J. Nucl. Mater.*, 336(2):331–368, 2005.
- [18] B Cox. Environmentally-induced cracking of zirconium alloys, a review. *J. Nucl. Mater.*, 170(1):1–23, 1990.
- [19] Arthur T Motta, Adrien Couet, and Robert J Comstock. Corrosion of zirconium alloys used for nuclear fuel cladding. *Annu. Rev. Mater. Res.*, 45:311–343, 2015.

- [20] David John Young. *High temperature oxidation and corrosion of metals*, volume 1. Elsevier, 2008.
- [21] Tamer El Maaddawy and Khaled Soudki. A model for prediction of time from corrosion initiation to corrosion cracking. *Cement and concrete composites*, 29(3):168–175, 2007.
- [22] TR Allen, RJM Konings, and AT Motta. 5.03 corrosion of zirconium alloys. *Comprehensive nuclear materials*, pages 49–68, 2012.
- [23] Patrick Jacques, Florence Lefebvre, and Clément Lemaignan. Deformation–corrosion interactions for zr alloys during i-scc crack initiation: part i: chemical contributions. *Journal of nuclear materials*, 264(3):239–248, 1999.
- [24] GS Frankel. *Fundamentals of Corrosion Kinetics*, pages 17–32. Springer, 2016.
- [25] S Kass. Aqueous corrosion of the zircaloys at low temperatures. *J. Nucl. Mater.*, 29(3):315–321, 1969.
- [26] Craig M Eucken, Peter T Finden, Siegrun Trapp-Pritsching, and Hans G Weidinger. Influence of chemical composition on uniform corrosion of zirconium-base alloys in autoclave tests. In *Zirconium in the Nuclear Industry: Eighth International Symposium*. ASTM International, 1989.
- [27] Patrick Jacques, Florence Lefebvre, and Clement Lemaignan. Deformation corrosion interactions for zr alloys during i scc crack initiation: Part ii: Localised stress and strain contributions. *Journal of nuclear materials*, 264(3):249–256, 1999.
- [28] K. Forsberg, M. Limback, and A. R. Massih. A model for uniform zircaloy clad corrosion in pressurized water reactors. *Nucl. Eng. Des.*, 154(2):157–168, 1995.
- [29] Benjamin Lustman and Frank Kerze. *The metallurgy of zirconium*, volume 4. McGraw-Hill Book Company, 1955.
- [30] Ece Alat, Jing Hu, Douglas Wolfe, and Arthur Motta. Corrosion and ion irradiation behavior of ceramic-coated nuclear fuel cladding. In *Zirconium in the Nuclear Industry: 19th International Symposium*, pages 149–171. ASTM International, 2021.
- [31] Naiming Lin, Qiang Liu, Jiaojuan Zou, Dali Li, Shuo Yuan, Zhihua Wang, and Bin Tang. Surface damage mitigation of ti6al4v alloy via thermal oxidation for oil and gas exploitation application: characterization of the microstructure and evaluation of the surface performance. *RSC advances*, 7(22):13517–13535, 2017.
- [32] George P Sabol and Gerry D Moan. *Zirconium in the nuclear industry: twelfth international symposium*, volume 1354. ASTM International, 2000.
- [33] Michael Reyes, Asghar Aryanfar, Sun Woong Baek, and Jaime Marian. Multilayer interface tracking model of zirconium clad oxidation. *J. Nucl. Mater.*, 509:550–565, 2018.

- [34] Arthur T Motta, Laurent Capolungo, Long-Qing Chen, Mahmut Nedim Cinbiz, Mark R Daymond, Donald A Koss, Evrard Lacroix, Giovanni Pastore, Pierre-Clément A Simon, Michael R Tonks, et al. Hydrogen in zirconium alloys: A review. *Journal of Nuclear Materials*, 518:440–460, 2019.
- [35] Michael Preuss. A review of early findings within the collaborative research programme muzic: Mechanistic understanding of zirconium corrosion. In *Zirconium in the Nuclear Industry: 19th International Symposium*. ASTM International, 2021.
- [36] Jian Li, M Elboujdaini, Bingyan Fang, RW Revie, and Michael W Phaneuf. Microscopy study of intergranular stress corrosion cracking of x-52 line pipe steel. *Corrosion*, 62(4):316–322, 2006.
- [37] Michel Mermoux and Christian Duriez. Raman imaging in corrosion science: High-temperature oxidation of the zirconium alloys used in the nuclear industry as an example. *Journal of Raman Spectroscopy*, 52(12):2131–2159, 2021.
- [38] AR Khasanova. Corrosion cracking under main pipelines stress. In *Journal of Physics: Conference Series*, volume 2176, page 012051. IOP Publishing, 2022.
- [39] Kamila Wilczynska, Matthew Bono, David Le Boulch, Marion Fregonese, Valérie Chabretou, Nathanael Mozzani, and Laureline Barbie. Development and validation of a new experimental device for studies of iodine stress corrosion cracking of zirconium alloys. In *19th International Conference on Environmental Degradation of Materials in Nuclear Power Systems-Water Reactors*, 2019.
- [40] M Kimura, N Totsuka, T Kurisu, K Amano, J Matsuyama, and Y Nakai. Sulfide stress corrosion cracking of line pipe. *Corrosion*, 45(4):340–346, 1989.
- [41] Benoit Gwinner, F Balbaud-Célérrier, Pierre Fauvet, Nathalie Gruet, Pierre Laghoutaris, Frédéric Miserque, and Raphael Robin. A step towards a better understanding of corrosion of zirconium in nitric acid with additions of fluorine: Focus on the role of the presence of an initial oxide film. *Corrosion Science*, 201:110284, 2022.
- [42] Yusha Li, Changchun Ge, Yanhong Liu, Guangbin Li, Xiaoxu Dong, Zongxing Gu, and Yingchun Zhang. Influencing factors and mechanism of iodine-induced stress corrosion cracking of zirconium alloy cladding: A review. *International Journal of Minerals, Metallurgy and Materials*, 29(4):586–598, 2022.
- [43] Xian-Feng Ma, Ya-Wen Wu, Jie Tan, Chui-Yi Meng, Liu Yang, Wei-An Dang, and Xiu-Jie He. Evaluation of corrosion and oxidation behaviors of tialcrn coatings for nuclear fuel cladding. *Surface and Coatings Technology*, 358:521–530, 2019.
- [44] QS Chen, CH Liu, JP Long, J Wang, RQ Zhang, HY Yang, W Zhang, FY Yao, S Zhao, and Q Zhang. Microstructure and corrosion characteristics of creufemoni hea coatings with different compositions in high-temperature and high-pressure water. *Materials Research Express*, 6(8):086511, 2019.

- [45] Xiangyang Sun, Feng Gong, Menglong Hao, Lei Wu, Chunyu Yin, Zhipeng Sun, and Rui Xiao. Enhanced thermal transport and corrosion resistance by coating vertically-aligned graphene on zirconium alloy for nuclear reactor applications. *Applied Surface Science*, 582:152484, 2022.
- [46] Byoung-Ho Choi, Alexander Chudnovsky, and Kalyan Sehanobish. Stress corrosion cracking in plastic pipes: observation and modeling. *International Journal of Fracture*, 145(1):81–88, 2007.
- [47] S Mohanty, S Majumdar, and K Natesan. A review of stress corrosion cracking/fatigue modeling for light water reactor cooling system components. *Argonne, IL: Nuclear Engineering Division Argonne National Laboratory*, 2012.
- [48] Xianglong Guo, Junqiang Lu, Ping Lai, Zhao Shen, Wenhua Zhuang, Zhongli Han, Lefu Zhang, and Sergio Lozano-Perez. Understanding the fretting corrosion mechanism of zirconium alloy exposed to high temperature high pressure water. *Corrosion Science*, 202:110300, 2022.
- [49] Chongchong Tang, Mirco Große, Sven Ulrich, Michael Klimenkov, Ute Jäntschi, Hans Jürgen Seifert, Michael Stüber, and Martin Steinbrück. High-temperature oxidation and hydrothermal corrosion of textured cr2alc-based coatings on zirconium alloy fuel cladding. *Surface and Coatings Technology*, 419:127263, 2021.
- [50] Helmut Mehrer. Diffusion in solids under pressure. In *Defect and Diffusion Forum*, volume 309, pages 91–112. Trans Tech Publ, 2011.
- [51] Fu-Zhen Xuan, Shan-Shan Shao, Zhengdong Wang, and Shan-Tung Tu. Coupling effects of chemical stresses and external mechanical stresses on diffusion. *Journal of Physics D: Applied Physics*, 42(1):015401, 2008.
- [52] RL De Orio, Hajdin Ceric, and Siegfried Selberherr. Physically based models of electromigration: From black's equation to modern tcad models. *Microelectronics Reliability*, 50(6):775–789, 2010.
- [53] Melchers Ahammed and RE Melchers. Reliability estimation of pressurised pipelines subject to localised corrosion defects. *International Journal of Pressure Vessels and Piping*, 69(3):267–272, 1996.
- [54] Shu-Xin Li, Shu-Rong Yu, Hai-Long Zeng, Jian-Hua Li, and Rui Liang. Predicting corrosion remaining life of underground pipelines with a mechanically-based probabilistic model. *Journal of Petroleum Science and Engineering*, 65(3-4):162–166, 2009.
- [55] TA Bubenik, RJ Olson, DR Stephens, and RB Francini. Analyzing the pressure strength of corroded line pipe. In *PROCEEDINGS OF THE INTERNATIONAL CONFERENCE ON OFFSHORE MECHANICS AND ARCTIC ENGINEERING*, pages 225–225. American Society of Mechanical Engineers, 1992.
- [56] Felipe Alexander Vargas Bazán and André Teófilo Beck. Stochastic process corrosion growth models for pipeline reliability. *Corrosion Science*, 74:50–58, 2013.

- [57] Peter R Bergethon. Flow in a chemical potential field: diffusion. In *The Physical Basis of Biochemistry*, pages 445–454. Springer, 1998.
- [58] IA Blech and Conyers Herring. Stress generation by electromigration. *Applied Physics Letters*, 29(3):131–133, 1976.
- [59] Markus Ganser, Felix E Hildebrand, Markus Klinsmann, Matthias Hanauer, Marc Kamlah, and Robert M McMeeking. An extended formulation of butler-volmer electrochemical reaction kinetics including the influence of mechanics. *Journal of the Electrochemical Society*, 166(4):H167, 2019.
- [60] Cristina O De González and Eduardo A García. Determination of the diffusion coefficients of oxygen in zirconium by means of xps. *Applied surface science*, 44(3):211–219, 1990.
- [61] Allen J. Bard and Larry R. Faulkner. *Electrochemical methods: fundamentals and applications*. 2 New York: Wiley, 1980., 1980.
- [62] Ralph H. Nielsen, James H. Schlewitz, Henry Nielsen, and Updated by Staff. Zirconium and zirconium compounds. *Kirk-Othmer Encyclopedia of Chemical Technology*, 2000.
- [63] David R Lide. *CRC handbook of chemistry and physics*, volume 85. CRC press, 2004.
- [64] Stephen D Cramer, Bernard S Covino Jr, Charles Moosbrugger, Bonnie R Sanders, Gayle J Anton, Nancy Hrivnak, Jill Kinson, Carol Polakowski, Kathryn Muldoon, Scott D Henry, et al. *ASM handbook*, volume 13. ASM international Materials Park, Ohio, 2003.
- [65] James J Duderstadt and Louis J Hamilton. *Nuclear reactor analysis*. Wiley, 1976.
- [66] XY Zhang, MH Shi, C Li, NF Liu, and YM Wei. The influence of grain size on the corrosion resistance of nanocrystalline zirconium metal. *Materials Science and Engineering: A*, 448(1-2):259–263, 2007.
- [67] F Al Gabr, J Ferrandis, D Baron, and P Chantoin. Pressure and composition of gas mixtures in fuel rods for pressurised water reactors by an ultrasonic sensor. *International conference on WWER fuel performance, modelling and experimental support, Varna, Bulgaria*, 2003.
- [68] R Kirchheim. Stress and electromigration in al-lines of integrated circuits. *Acta Metallurgica et Materialia*, 40(2):309–323, 1992.
- [69] E Hillner, DG Franklin, and JD Smee. Long-term corrosion of zircaloy before and after irradiation. *Journal of nuclear materials*, 278(2-3):334–345, 2000.
- [70] Philippe F Weck, Eunja Kim, Veena Tikare, and John A Mitchell. Mechanical properties of zirconium alloys and zirconium hydrides predicted from density functional perturbation theory. *Dalton Transactions*, 44(43):18769–18779, 2015.
- [71] J Chakrabarty and WJ Drugan. Theory of plasticity. *J. Appl. Mech.*, 55:253, 1988.

- [72] Saragosa Silvano. Mathematical model of the lame’problem for simplified elastic theory applied to controlled-clearance pressure balances. *arXiv preprint arXiv:1007.0813*, 2010.
- [73] Asghar Aryanfar, William Goddard III, and Jaime Marian. Constriction percolation model for coupled diffusion-reaction corrosion of zirconium in pwr. *Corrosion Science*, 158:108058, 2019.
- [74] Chunhua Xu and Wei Gao. Pilling-bedworth ratio for oxidation of alloys. *Material Research Innovations*, 3(4):231–235, 2000.
- [75] D.G. Peters, H.R. in: Franklin and R.B. (Eds.) Adamson. Sixth international symposium on zirconium in the nuclear industry. page 507. ASTM STP 824, American Society for Testing and Materials, 1984.
- [76] S.B. Dalgaard. Extended abstracts of the electrochem- ical society, washington, dc, usa. page 82. ASTM STP 824, 2-7 May 1976.
- [77] F Garzarolli, W Jung, H Schoenfeld, AM Garde, GW Parry, and PG Smerd. Waterside corrosion of zircaloy fuel rods. final report. Technical report, Kraftwerk Union AG, 1982.
- [78] H Stehle, W Kaden, and R Manzel. External corrosion of cladding in pwrs. *Nuclear Engineering and Design*, 33(2):155–169, 1975.
- [79] Howard C Berg. Diffusion: microscopic theory. In *Random walks in biology*, pages 5–16. Princeton University Press, 2018.

Appendix

Herein, we present the detailed steps for establishing the relationships shown in the article.

1. Elastic Stress σ_{EL} (Eqn. 7)

Imposing the internal and external pressures P_I and P_O , the radial σ_r and hoop σ_θ elastic stresses develop, as shown in the Figure 2a which are only function of radius r due to polar symmetry. Cutting-out the infinitesimal element shown in the Figure 2b the balance relationships in horizontal direction would be:

$$\sum F_x = 0$$

therefore:

$$\left(\sigma_r + \frac{\partial \sigma_r}{\partial r} dr \right) \cdot (r + dr) d\theta - \sigma_r \cdot r d\theta - 2\sigma_\theta \cdot dr \cdot \frac{d\theta}{2} = 0$$

where by simplification and ignoring the higher orders terms, we arrive at Lamé's relationship as [71, 72]:

$$\frac{\partial \sigma_r}{\partial r} + \frac{\sigma_r - \sigma_\theta}{r} = 0$$

Regarding the strain ϵ , if u is the infinitesimal displacement in the radial direction, from the Hook's generalized law one gets [71]:

$$\begin{cases} \epsilon_r = \frac{du}{dr} = \frac{1}{E} (\sigma_r - \nu \sigma_\theta) \\ \epsilon_\theta = \frac{u}{r} = \frac{1}{E} (\sigma_\theta - \nu \sigma_r) \end{cases}$$

Solving for the radial σ_r and hoop σ_θ stresses and replacing in terms of the infinitesimal displacement u one gets:

$$\begin{cases} \sigma_r = \frac{E}{1 - \nu^2} \left(\frac{du}{dr} + \nu \frac{u}{r} \right) \\ \sigma_\theta = \frac{E}{1 - \nu^2} \left(\frac{u}{r} + \nu \frac{du}{dr} \right) \end{cases} \quad (39)$$

replacing the Equations 39 into the compatibility Equation 5 and simplifying we get:

$$\frac{d}{dr} \left(\frac{1}{r} \frac{d}{dr} (u \cdot r) \right) = 0$$

where integrating leads to:

$$u = C_1 r + \frac{C_2}{r}$$

From the Figure 2a, assuming the $\{R_I, R_O\}$ are inner and outer radii the pipe respectively and assigning the boundary conditions for the compressive stresses as $\sigma_r(R_I) = -P_I$ and $\sigma_r(R_O) = -P_O$,

the hoop stress σ_P is finally obtained as:

$$\begin{cases} \sigma_r = A + \frac{B}{r^2} \\ \sigma_\theta = A - \frac{B}{r^2} \end{cases} \quad (40)$$

where A and B are constants obtained by the following relationships:

$$\begin{cases} A = \frac{P_I R_I^2 - P_O R_O^2}{R_O^2 - R_I^2} \\ B = \frac{R_I^2 R_O^2 (P_O - P_I)}{R_O^2 - R_I^2} \end{cases} \quad (41)$$

Since the compressive stress causing the failure is the hoop direction, therefore $\sigma_P = \sigma_\theta$ and hence the Equation 7 is obtained as:

$$\sigma_P = \frac{P_I R_I^2 - P_O R_O^2}{R_O^2 - R_I^2} + \left(\frac{R_I^2 R_O^2 (P_O - P_I)}{R_O^2 - R_I^2} \right) \frac{1}{r^2} \quad (42)$$

which is the compressive stress generated by the bounded-ness in the azimuthal (i.e hoop) direction.

2. Corrosion Stress (Eqn. 17)

$$\begin{aligned} \sigma_{EL} &= K \frac{\nu}{1+\nu} \frac{dA}{A} \\ &= K \frac{\nu}{1+\nu} \int_0^s \frac{2\pi \left(R_I - \frac{R-1}{R} s \right) \frac{R-1}{R} ds}{\pi \left(R_O^2 - \left(R_I - \frac{R_{PB}-1}{R_{PB}} s \right)^2 \right)} \\ &= K \frac{\nu}{1+\nu} \int_0^s \left(\frac{-\frac{R-1}{R}}{R_O + R_I - \frac{R_{PB}-1}{R_{PB}} s} + \frac{\frac{R-1}{R}}{R_O - R_I + \frac{R_{PB}-1}{R_{PB}} s} \right) ds \\ &= K \frac{\nu}{1+\nu} \left(\ln \left(R_O + R_I - \frac{R-1}{R} s \right) \Big|_0^s + \ln \left(R_O - R_I + \frac{R-1}{R} s \right) \Big|_0^s \right) \\ &= K \frac{\nu}{1+\nu} \left(\ln \left(1 - \frac{R-1}{R} \frac{s}{R_O + R_I} \right) + \ln \left(1 + \frac{R-1}{R} \frac{s}{R_O - R_I} \right) \right) \\ &= K \frac{\nu}{1+\nu} \left(\ln \left(1 + \frac{R-1}{R} \frac{s}{R_O - R_I} - \frac{R-1}{R} \frac{s}{R_O + R_I} + \left(\frac{R-1}{R} \right)^2 \frac{s^2}{R_O^2 - R_I^2} \right) \right) \\ &= K \frac{\nu}{1+\nu} \ln \left(1 + \frac{R-1}{R} \left(\frac{2R_I}{R_O^2 - R_I^2} \right) s + \left(\frac{R-1}{R} \right)^2 \frac{s^2}{R_O^2 - R_I^2} \right) \end{aligned}$$

3. Corrosion Stress (Eqn. 21)

$$\begin{aligned}
\sigma_{EL} &= K \frac{\nu}{1+\nu} \int_0^s \frac{2\pi \left(R_O + \frac{R-1}{R} s \right) \frac{R-1}{R} ds}{\pi \left(\left(R_O + \frac{R-1}{R} s \right)^2 - R_I^2 \right)} \\
&= K \frac{\nu}{1+\nu} \int_0^s \left(\frac{\frac{R-1}{R}}{R_O + \frac{R-1}{R} s - R_I} + \frac{\frac{R-1}{R}}{R_O + \frac{R-1}{R} s + R_I} \right) ds \\
&= K \frac{\nu}{1+\nu} \left(\ln \left(1 + \frac{R-1}{R} \frac{s}{R_O - R_I} \right) + \ln \left(1 + \frac{R-1}{R} \frac{s}{R_O + R_I} \right) \right) \\
&= K \frac{\nu}{1+\nu} \ln \left(1 + \frac{R-1}{R} \left(\frac{2R_O}{R_O^2 - R_I^2} \right) s + \left(\frac{R-1}{R} \right)^2 \frac{s^2}{R_O^2 - R_I^2} \right)
\end{aligned}$$

4. Equation 23:

Translating the Equation 22 into 1D radial direction, we get:

$$\begin{aligned}
\left(\frac{dC}{dt} \right)_{\text{Diff}} &= D \nabla \cdot \left(\nabla C + \frac{f\Omega}{R_u T} C \nabla \sigma_r \right) \\
&= D \frac{\partial}{\partial r} \left(\frac{\partial C}{\partial r} + \frac{f\Omega}{R_u T} C \frac{\partial \sigma_r}{\partial r} \right)
\end{aligned}$$

The σ_r is obtained from Equations 40 and 41, therefore: $\frac{\partial \sigma_r}{\partial r} = -\frac{2B}{r^3}$, replacing gives:

$$\begin{aligned}
\left(\frac{dC}{dt} \right)_{\text{Diff}} &= D \frac{\partial}{\partial r} \left(\frac{\partial C}{\partial r} - \frac{2f\Omega C B}{R_u T r^3} \right) \\
&= D \left(\frac{\partial^2 C}{\partial r^2} - \frac{2f\Omega B}{R_u T r^3} \frac{\partial C}{\partial r} + 6 \frac{f\Omega B}{R_u T r^4} C \right) \\
&= D \frac{\partial^2 C}{\partial r^2} + \alpha(r) \frac{\partial C}{\partial r} + \beta(r) C
\end{aligned}$$

and the coefficients α and β are obtained respectively as:

$$\alpha(r) = -\frac{2Df\Omega B}{R_u T r^3}, \quad \beta = 6 \frac{fD\Omega B}{R_u T r^4}$$

6. Equation 29:

In order to have a stable solution, we need to have $Q_1 > 0$, hence:

$$1 - \frac{2D\delta t}{\delta r^2} + \frac{\alpha(r)\delta t}{\delta r} + \beta(r)\delta t > 0$$

replacing the α and β values gives:

$$1 - \frac{2D\delta t}{\delta r^2} - \frac{2Df\Omega B}{R_u Tr^3} \frac{\delta t}{\delta r} + \frac{6fD\Omega B}{R_u Tr^4} \delta t > 0$$

which means that:

$$\delta t < \left(\frac{2D}{\delta r^2} + \frac{2fD\Omega B}{R_u Tr^3 \delta r} - \frac{6fD\Omega B}{R_u Tr^4} \right)^{-1} \checkmark$$